

UC Irvine

UC Irvine Previously Published Works

Title

Segmentation of polarimetric synthetic aperture radar data

Permalink

<https://escholarship.org/uc/item/3vx4x64j>

Journal

IEEE Transactions on Image Processing, 1(3)

ISSN

1057-7149

Authors

Rignot, E
Chellappa, R

Publication Date

1992-07-01

DOI

10.1109/83.148603

Copyright Information

This work is made available under the terms of a Creative Commons Attribution License, available at <https://creativecommons.org/licenses/by/4.0/>

Peer reviewed

Segmentation of Polarimetric Synthetic Aperture Radar Data

Eric Rignot and Rama Chellappa, *Fellow, IEEE*

Abstract—A statistical image model is proposed for segmenting polarimetric synthetic aperture radar (SAR) data into regions of homogeneous and similar polarimetric backscatter characteristics. A model for the conditional distribution of the polarimetric complex data is combined with a Markov random field representation for the distribution of the region labels to obtain the posterior distribution. Optimal region labeling of the data is then defined as maximizing the posterior distribution of the region labels given the polarimetric SAR complex data (maximum a posteriori (MAP) estimate). An implementation of the MAP technique on a parallel optimization network is presented. A fast alternative solution is also considered. Two procedures for selecting the characteristics of the regions are then discussed: one is supervised and requires training areas, the other is unsupervised and is based on the multidimensional clustering of the logarithm of the parameters composing the polarimetric covariance matrix of the data. Results using *real* multilook polarimetric SAR complex data are given to illustrate the potential of the two selection procedures and evaluate the performance of the MAP segmentation technique. The impact of reducing the dimension of the polarimetric measurements on segmentation accuracy is also investigated. The results indicate that dual polarization SAR data may yield almost similar segmentation results as the fully polarimetric SAR data.

I. INTRODUCTION

THE electromagnetic wave transmitted by a radar system is characterized by its frequency and its polarization state which describes the relative motion of the vector representing the electrical field when the wave moves towards an observer. Conventional radars use the same antenna polarization configuration for both transmission and reception of the electromagnetic signal and operate at a fixed polarization. These systems do not permit a complete characterization of the mechanisms of interaction of the electromagnetic wave when the surface and the depolarization properties of natural targets cannot be studied. In recent years, fully polarimetric radars have been developed [1] that acquire all the information contained in the radar response. The radar signal is decom-

posed into two orthogonal signals, one horizontal, the other vertical (Fig. 1), that are received and processed independently in separate channels. By using various combinations of horizontal and/or vertical polarization configurations of the transmission and reception ends, the complete polarimetric scattering matrix is measured for each resolution element of the imaged scene. The recorded elements of the scattering matrices can then be combined to synthesize any type of transmit/receive polarization configuration and study the variation with polarization of the intensity and phase of the backscatter response of natural targets [2].

Polarimetric synthetic aperture radar (SAR) data help researchers understand and quantify the scattering properties of natural scenes and their variability under different conditions better than single polarization SAR data. Along with the diffusion of this type of radar data among the scientific community, a number of polarimetric radar analysis techniques have been reported in the literature to measure and characterize the polarization response of natural targets [2], to maximize the contrast between targets based on polarimetric filtering [1], or to classify SAR data based on the type of scattering mechanisms [3]. SAR data also received some attention recently in terms of segmenting them into edges [4] or regions [5], [6], [7]. In [7], a method was proposed for segmenting single look single polarization SAR complex data into regions of homogeneous and similar backscatter characteristics. In this paper, we consider the case of multilook multipolarization SAR complex data and evaluate the performance of the segmentation technique using *real* polarimetric SAR data.

There is a considerable interest in developing segmentation procedures for polarimetric SAR data as they may yield a more quantitative, time, and cost effective analysis of the data than visual interpretation of photo products. Further, they may facilitate the inference of geophysical parameters from the surface and the near surface (e.g., surface roughness, soil moisture content, dielectric constant, etc.) as model inversion techniques are computationally more efficient when applied on the polarimetric backscatter characteristics of large homogeneous regions than on a pixel by pixel basis [8].

A maximum likelihood (ML) polarimetric classifier was derived by Kong *et al.* [9] assuming that the polarimetric complex data are multivariate circular Gaussian. As confusion may occur between regions when the radar re-

Manuscript received April 15, 1991; revised September 16, 1991. This work was supported by the National Aeronautics and Space Administration at the Jet Propulsion Laboratory, California Institute of Technology and by the Air Force Office of Scientific Research under Contract F49620-92-J0130.

E. Rignot is with the Jet Propulsion Laboratory, California Institute of Technology, Pasadena, CA 91109.

R. Chellappa is with the Department of Electrical Engineering, Center for Automation Research and the Institute for Advanced Computer Studies, University of Maryland, College Park, MD 20742.

IEEE Log Number 9200287.

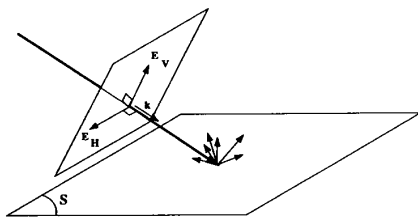


Fig. 1. Definition of H and V in a polarimetric imaging radar. E_H is the horizontal component of the electrical field, k is the wave vector, and S is the surface imaged by the radar.

sponse significantly varies with the incidence angle [10], a normalized ML classifier was derived by Yueh *et al.* [11] which, in some cases, produces better results than the unnormalized classifier. Yet, the resulting segmentation maps are not satisfactory and appear noisy. Van Zyl and Burnette [12] proposed a subsequent improvement of the results using a simple deterministic relaxation technique that locally estimates the probability of the regions and smoothes out the ML segmentation map. In our work, a more elegant framework is given based on a composite image model for the polarimetric data. Each sample point or pixel is characterized by two attributes: 1) a polarimetric measurement vector; 2) a region label which identifies the region to which the pixel belongs. A model for the posterior distribution of the region labels, given the polarimetric measurement vectors, is proposed and optimal region labeling of the pixels is defined as maximizing the posterior distribution of the region labels (maximum *a posteriori* (MAP) estimate). The MAP method is implemented on a parallel optimization network as in [7], [13]. A fast alternative solution to the MAP estimate is also considered. Several examples using *real* multilook polarimetric SAR data are given to illustrate the potential of the method and evaluate its accuracy. Additionally, two procedures for selecting the polarimetric characteristics of the regions are discussed: one is supervised and requires training areas, the other is unsupervised and is based on the multidimensional clustering of the logarithm of the parameters composing the polarimetric covariance matrix. Examples using both techniques are given and discussed. Finally, the impact of reducing the dimension of the polarimetric measurements on classification accuracy is evaluated. Classification results using single, dual, and fully polarimetric SAR data are compared.

The paper is organized as follows. In Section II, a model for the conditional distribution of the polarimetric SAR measurements is discussed. Section III presents a model for the distribution of the region labels using a Markov random field. The two models are combined in Section IV to obtain the posterior distribution of the region labels given the polarimetric SAR data. Optimal region labeling is then defined as maximizing the posterior distribution of the region labels. The implementation of the method on a parallel optimization network is discussed in Section V. In Section VI, two procedures for selecting the polarimetric characteristics of the regions are

presented. Section VII gives several examples using *real* multilook polarimetric SAR complex data to illustrate the potential of the selection procedures and evaluate the performance of the MAP technique. Section VIII concludes the paper.

II. STATISTICS OF POLARIMETRIC SAR DATA

In this section a model for the conditional distribution of the polarimetric SAR complex data, given the region labels, is presented. The region label of pixel site s of the image plane is designated as $L_s = l$ with $l \in \{1, \dots, K\}$ where K is the number of regions, X_s denotes the single look polarimetric measurement vector at pixel site s , i.e., the vector of the three single look polarimetric complex amplitudes measured at site s by the polarimetric radar:

$$X_s = [HH, HV, VV]_s \quad (1)$$

where, for instance

$$HV = |HV| \exp \{i\phi_{HV}\}. \quad (2)$$

$|HV|$ and ϕ_{HV} are, respectively, the amplitude and the phase of the electromagnetic return at the HV polarization. The HV amplitude, or cross-polarized return, is the complex amplitude of the V -polarized response given that the transmitted signal is H -polarized. The HH and VV amplitudes are referred as the copolarized returns. The VH return is not present in (1) as it is symmetrized with the HV return during compression and calibration of the data based on the reciprocity principle [1]. The conditional distribution of the single look polarimetric measurement vector X_s given its region label L_s is circular Gaussian [9]:

$$p(X_s/L_s = l) = \frac{1}{\pi^3} \exp \{-X_s^* C_l^{-1} X_s^T - \log |C_l|\}. \quad (3)$$

The superscript $*$ denotes complex conjugation and the superscript T means the transpose of the vector. The 3 by 3 complex matrix $C_l = \langle X^{*T} X \rangle_l$, where $\langle \rangle$ denotes ensemble averaging, is the polarimetric covariance matrix of the data in region l .

The circular Gaussian model (3) assumes that each region has stationary backscatter statistics, i.e., the covariance matrix C_l is translation invariant. The only source of spatial variability of the SAR signal at different polarizations and within a homogeneous region is image speckle. In the case of the real polarimetric SAR data used in this paper, measures of local statistical characteristics of the signal such as its variance and its correlation coefficient reveal that the Gaussian assumption is quite reasonable. Yet, other examples have been reported in the literature where the SAR signal is also significantly modulated by a spatial variability of the backscatter coefficient of the imaged surface, in which case multivariate K -distributions may better model the statistics of the polarimetric SAR data [14], [15].

The direct evaluation of (3) at each pixel location involves prohibitive calculations of the Hermitian form

$(X_s^* C_l^{-1} X_s^T)$. A simplification is possible in the presence of azimuthally symmetric targets (the case of a large variety of natural targets), in that the HV amplitude is uncorrelated with the HH and VV complex amplitudes [16] and the covariance matrix is

$$C_l = \sigma_l \begin{pmatrix} 1 & 0 & \rho_l \sqrt{\gamma_l} \\ 0 & \epsilon_l & 0 \\ \rho_l^* \sqrt{\gamma_l} & 0 & \gamma_l \end{pmatrix} \quad (4)$$

where

$$\begin{aligned} \sigma_l &= \langle |HH|^2 \rangle_l \\ \epsilon_l &= \frac{\langle |HV|^2 \rangle_l}{\langle |HH|^2 \rangle_l} \\ \gamma_l &= \frac{\langle |VV|^2 \rangle_l}{\langle |HH|^2 \rangle_l} \\ \rho_l &= \frac{\langle HHVV^* \rangle_l}{\sqrt{\langle |HH|^2 \rangle_l \langle |VV|^2 \rangle_l}}. \end{aligned} \quad (5)$$

In (4), C_l can be inverted analytically, leading to

$$\begin{aligned} p(X_s/L_s = l) &= \frac{1}{\pi^3} \exp \left\{ -\frac{|HH|^2}{\sigma_l(1 - |\rho_l|^2)} \right. \\ &\quad - \frac{|HV|^2}{\sigma_l \epsilon_l} - \frac{|VV|^2}{\sigma_l \gamma_l (1 - |\rho_l|^2)} \\ &\quad + 2 \frac{\text{Re}(HHVV^* \rho_l)}{\sigma_l \sqrt{\gamma_l} (1 - |\rho_l|^2)} \\ &\quad \left. - \log [\sigma_l^3 \epsilon_l \gamma_l (1 - |\rho_l|^2)] \right\} \quad (6) \end{aligned}$$

where $\phi_{HHV} = \phi_{HH} - \phi_{VV}$, Re denotes the real part of a complex number, and ϕ_{ρ_l} is the phase of ρ_l . The evaluation of (6) now requires a much smaller number of operations.

To improve the process of assigning a region label to each pixel site s , one can replace the conditional distribution of a single polarimetric measurement vector (6) by the joint conditional distribution of a small set of polarimetric measurement vectors contained in a neighborhood N_s of site s . Region labeling will then exploit the additional polarimetric information provided by the neighbors of s . Because of the presence of the SAR system impulse response, typically two pixels wide, these measurements are slightly correlated. In [7], following an analysis of the correlation properties of single look single polarization SAR complex data, an accurate analytical expression of their joint distribution function was derived. Yet, in this paper, we will assume that the N polarimetric measurement vectors $X_s = [X_1, \dots, X_N]$ contained in N_s are spatially nearly uncorrelated, i.e., conditionally independent as they are circular Gaussian, and the conditional distribution of X_s is the product of the conditional distributions of the X_i 's. Several reasons preclude the use of a

spatially correlated model. The first one is that the polarimetric covariance matrix of the joint measurements would not have an inverse with a simple closed form analytical expression, thereby severely increasing the computational cost of the joint distribution approach. Secondly, in the case of multilook SAR data samples, the correlation properties of the signal are much more difficult to track analytically [17]. Thirdly, tests using both simulated and real single look single polarization SAR complex data have already shown that the improvement in segmentation accuracy resulting from a spatially correlated measurement model is only on the order of a few percentage points [17]. Indeed, the uncorrelated assumption may seem contradictory to the fact that we want to use contextual information in the segmentation technique, i.e., some form of spatial correlation between pixel elements, but this is exactly what the model for representing the interactions between neighboring region labels does (Section III), and the segmentation results obtained indicate that it is not necessary to also account for the spatial correlation of individual pixel elements in the SAR measurement model.

In addition to the uncorrelated assumption, we view the polarimetric data array as composed of $M \times M$ (where M is the image size) overlapping windows N_s such that each of these windows is homogeneous, i.e., all pixels have the same region label. The conditional distribution of X_s , therefore, only depends on the region label L_s . The conditional distribution of the entire polarimetric data array X given the entire region label array L is then expressed as

$$p(X/L) = \prod_s p(X_s/L_s) \quad (7)$$

with the conditional distribution of X_s in each window being

$$p(X_s/L_s = l) = \prod_{i \in N_s} p(X_i/L_i = l). \quad (8)$$

Using a Gibbs representation of (8), we have

$$p(X_s/L_s = l) = \frac{\exp \{-NU_1^s(X_s/L_s = l)\}}{\pi^{3N}} \quad (9)$$

where the energy function U_1^s is

$$\begin{aligned} U_1^s(X_s/L_s = l) &= \frac{|HH^N|^2}{\sigma_l(1 - |\rho_l|^2)} + \frac{|HV^N|^2}{\sigma_l \epsilon_l} \\ &\quad + \frac{|VV^N|^2}{\sigma_l \gamma_l (1 - |\rho_l|^2)} \\ &\quad - 2 \frac{\text{Re}(HHVV^* \rho_l)}{\sigma_l \sqrt{\gamma_l} (1 - |\rho_l|^2)} \\ &\quad + \log [\sigma_l^3 \epsilon_l \gamma_l (1 - |\rho_l|^2)] \quad (10) \end{aligned}$$

and

$$\begin{aligned} HH^N VV^{*N} &= \frac{1}{N} \sum_{i=1}^{i=N} HH_i VV_i^* \\ |HH^N|^2 &= \frac{1}{N} \sum_{i=1}^{i=N} |HH_i|^2. \end{aligned} \quad (11)$$

The operation of computing (11) is exactly equivalent to a multilook operation performed on N single look polarimetric SAR complex data samples [18], known as reducing image speckle, which demonstrates that the conditional joint distribution (9) provides better information about the polarimetric backscatter characteristics of site s than the conditional distribution (6). To compute (9) at each pixel location, either N single look polarimetric SAR complex data samples or one N -look polarimetric SAR complex data sample are necessary as each N -look polarimetric SAR complex measurement contains all the complex elements computed in (11). Hence, the segmentation technique described in this paper is applicable in a straightforward manner to the case of multilook polarimetric SAR complex data. The reader may note that the absolute phases of the polarimetric amplitudes, lost during the multilook operation, are not required as they do not appear in (10), which is an advantage resulting from the assumption that the single look data samples are spatially uncorrelated.

The ML approach proposed in [9] defines optimal region labeling of the data as maximizing the conditional distribution of the polarimetric measurement vector (3) at each pixel location. The results appear noisy and are not satisfactory for practical applications. One reason is that the regions are assumed to have equal probabilities which, locally, in the presence of a dominant region, is rarely correct, increases the classification error, and leaves pixels or ensembles of pixels isolated and not connected to a region. Another reason is that the information provided by neighboring region labels and polarimetric measurement vectors is ignored. Contextual information is fundamental to deriving appropriate image models for segmenting SAR data as neighboring surface elements of natural scenes usually have similar polarimetric characteristics, sometimes textured, that locally define homogeneous regions of similar physical attributes and smooth and straight boundaries. To capture this spatial organization of the data in a mathematical form, a statistical model for representing the interactions between neighboring region labels is included in our description of the polarimetric SAR data.

III. REGION LABELING USING A MARKOV RANDOM FIELD

Markov random fields (MRF) are both mathematically and computationally convenient for representing local interactions between neighboring pixel attributes. They can model the spatial extent, the structure, and the geometry of the interactions. They have an equivalent descrip-

tion in terms of Gibbs energy functions which provides a more practical way of describing the state of organization of physical attributes within a system than local probabilities. An example is the two-level Ising model [19] which defines a Gibbs energy consistent with the regularity observed in the orientation of the spin of atoms in ferromagnets as the spins tend to line up. A multilevel extension of this energy model is used in our work to model the distribution of the region labels. The multilevel Ising model is one of the simplest models describing the interactions between neighboring region labels as the region labeling is assumed isotropic and the degree of clustering of the region labels is independent of the region.

The conditional distribution of the region label L_s , given the region labels elsewhere, is only dependent on the region labels of an immediate neighborhood (Markovian property) and is expressed as

$$\begin{aligned} p(L_s = l/L_r, r \in N_s^o) \\ = \frac{1}{Z_2} \exp \{-NU_2^s(L_s = l/L_r, r \in N_s^o)\} \end{aligned} \quad (12)$$

where the Gibbs energy function U_2^s is

$$U_2^s(L_s = l/L_r, r \in N_s^o) = -\frac{\beta}{N} \sum_{r \in N_s} \delta_k(L_s - L_r). \quad (13)$$

The distribution of the entire region label array L is given as

$$p(L) \propto \exp \{\beta v\} \quad (14)$$

where v is the number of neighbor pairs having the same region label [20], β is a positive constant, δ_k is the Kronecker delta, N_s^o is a neighborhood of N elements excluding its center s , and Z_2 is a positive normalizing constant independent of l .

To be consistent with (9), the same neighborhood structure is selected for both modeling of the polarimetric complex amplitudes and the region labels. N_s is a 3 by 3 square box, i.e., a second-order neighborhood window. Higher order neighborhoods provide better smoothing of the data and segmentation accuracy within homogeneous areas but impair the detection of small structural details and also increase the classification error at the region boundaries [7].

The positive constant β encourages neighboring pixels to have the same region label and also determines the degree of clustering of the data. In [7], tests using simulated SAR data indicate that best segmentation results are obtained for β in the range of [1.0-1.6] independent of the data set. The value $\beta = 1.4$ was adopted in all our experiments. Larger values of β lead to excessive smoothing of the regions and leaking of region labels into neighboring regions, whereas $\beta = 0$ corresponds to the ML approach. Similar values of β have been found useful for segmenting textured incoherent optical images [13] and medical imagery [20].

IV. THE MAP CLASSIFIER

Using Bayes' theorem, the posterior distribution of the region label L_s given the single look polarimetric amplitudes X_s and the region labels L_r of a neighborhood N_s^o is

$$\begin{aligned} p(L_s = l/L_r, r \in N_s^o, X_s) \\ = \frac{p(L_s = l/L_r, r \in N_s^o)p(X_s/L_s = l)}{p(X_s)} \end{aligned} \quad (15)$$

since X_s and L_r are independent. As X_s is known, $p(X_s)$ is just a positive constant independent of the region labels. Using (9) and (12), we then have

$$\begin{aligned} p(L_s = l/L_r, r \in N_s^o, X_s) \\ \propto \exp \left\{ -NU_1^s(X_s/L_s = l) \right. \\ \left. - NU_2^s(L_s = l/L_r, r \in N_s^o) \right\}. \end{aligned} \quad (16)$$

The posterior distribution of the entire region label array L given the entire polarimetric array X , is

$$p(L/X) = \frac{p(L)p(X/L)}{p(X)}. \quad (17)$$

As X is known, $p(X)$ is just a positive constant. Using (7), (9), and (12), (17) is found to be proportional to

$$\begin{aligned} p(L/X) \propto \exp \left\{ -N \sum_s [U_1^s(X_s/L_s = l) \right. \\ \left. + U_2^s(L_s = l/L_r, r \in N_s^o)] \right\}. \end{aligned} \quad (18)$$

The estimate of L that maximizes (18) is the Bayes' most likely estimate of the region labels given the polarimetric data, or its MAP estimate. Expressed in terms of an energy function, the MAP estimate of L minimizes

$$E_{\text{MAP}} = \sum_s [U_1^s(X_s/L_s = l) + U_2^s(L_s = l/L_r, r \in N_s^o)]. \quad (19)$$

The energy functions U_1 and U_2 only depend on local conditions, i.e., local polarimetric amplitudes and region labels. It is consistent with the assumptions of our simplified image model.

In a Bayesian framework, other optimality criteria may be considered. In [21], the minimization of the posterior expected error rate was selected as the optimality criterion, leading to the maximum posterior marginal (MPM) algorithm. As it minimizes the expected number of misclassified pixels [21], the MPM estimate may be more appropriate than the MAP estimate for classifying natural scenes. Yet, in [7], by using simulated single look single polarization SAR complex data, we observed that the MAP estimate performs slightly better than the MPM estimate unless the intensity contrast between the regions is less than 0.5 dB. The result may seem counter-intuitive as MPM is expected to perform better [21]. A possible explanation is that, as is well known, MAP favors the use of a single region label for the entire scene, and therefore,

has a tendency to smooth out the results more than MPM which uses local decisions. As simulated data are composed of perfectly homogeneous regions, the tests favor the method that does more smoothing, i.e., MAP. In the case of real single look single polarization SAR data, the segmentation results shown in [7] were very similar and the lack of extensive ground truth information did not permit a confident ranking of the two methods. As the MAP criterion seems to perform extremely well and is much simpler to implement than the MPM criterion, it is selected as the optimality criterion in this paper. In the next section, we show how the minimization of the nonconvex MAP energy function (19) is carried out using a parallel optimization network.

V. IMPLEMENTATION OF THE MAP CLASSIFIER

The energy function minimized by a one-layer full interconnected Hopfield parallel optimization network [22] is expressed as

$$E_H = -\frac{1}{2} \sum_{i,j,l} \sum_{m,n,p} T_{i,j,l,m,n,p} V_{i,j,l} V_{m,n,p} - \sum_{i,j,l} I_{i,j,l} V_{i,j,l}. \quad (20)$$

$T_{i,j,l,m,n,p}$ are the interconnection weights of the nodes of the network, $V_{i,j,l}$ their output states, and $I_{i,j,l}$ their bias input currents. By comparing (19) and (20), if (i, j) are the image coordinates of pixel site s , and l is its region label, the weights of the corresponding network are

$$\begin{aligned} T_{i,j,l,m,n,p} &= 2 \frac{\beta}{N}, \quad \text{if } (m, n) \in N_{i,j}^o, \forall l = p \\ T_{i,j,l,m,n,p} &= 0, \quad \text{otherwise} \end{aligned} \quad (21)$$

the bias input currents are

$$I_{i,j,l} = U_1^{i,j}(X_{i,j}/L_{i,j} = l) \quad (22)$$

and the outputs of the nodes of the network are

$$\begin{aligned} V_{i,j,l} &= 1, \quad \text{if } L_{(i,j)} = l \\ V_{i,j,l} &= 0, \quad \text{otherwise.} \end{aligned} \quad (23)$$

Hence, only a simple change in notation is necessary to establish the correspondence between the energy function (19) and the energy function (20) minimized by a Hopfield parallel optimization network. The interconnection weights of the network only depend on the region labeling process (parameter β), and the bias input currents only depend on the polarimetric measurements. From one image to another, the network keeps the same structure and connectivity but receives different bias input currents. Further, the selection for each pixel (i, j) of the label l that produces the largest value of $I_{i,j,l}$ corresponds to the computation of the ML estimate of the region labels since the prior distribution (9) will be maximized. The ML solution also corresponds to $\beta = 0$.

Given the bias input currents and an initial region labeling configuration, the optimization network will evolve towards an equilibrium state solution for which E_H (i.e.,

E_{MAP}) is a minimum. During optimization, each pixel is visited in a random fashion to update its region label based on the current region labeling of other pixels and on its bias input currents. One iteration of the network corresponds to a number of visits equal to the number of pixels in the image. At equilibrium, the optimal region label of each pixel site (i, j) is read from the output state $V_{i,j,l}$ of the corresponding node.

To obtain a close approximate to the MAP estimate, a stochastic relaxation technique based on simulated annealing [23] guides the convergence of the network as in [7], [13]. The method requires several hundred iterations of the network and a few cooling cycles. An alternative strategy is to use the Iterative Conditional Modes (ICM's) algorithm of Besag [20], [13]. ICM converges in a few iterations, with no cooling cycles and no restrictions on the order of visiting of the pixels. However, instead of minimizing (18), ICM minimizes the posterior conditional distribution of the region labels at each pixel location (16). In [7], MAP was shown to significantly outperform ICM in the case of single look single polarization SAR data, and in [13] ICM was shown to be sensitive to the initial configuration of the network. Additional comparisons are provided in Section VII of this paper using real multilook polarimetric SAR data and an increasing number of regions. In fact, much light can be shed on what ICM does by considering the case where the pixels are visited in a random fashion with no simultaneous updating of contiguous pixels. ICM is then exactly equivalent to the zero temperature solution of (19), i.e., yields a poorer local minimum than the one obtained using simulated annealing, easily gets stuck in local minima close to the ML solution when initialized with the ML solution, and is more sensitive to an increase in size of the search space. The maximization of (16) does not seem to be an appropriate objective function because it misses a measure of the degree of equilibrium of each region labeling configuration and a joint probability law over various possible labeling configurations.

VI. SELECTION OF THE POLARIMETRIC FEATURE VECTORS

According to the circular Gaussian model (3), the polarimetric complex covariance matrix C_l completely characterizes a class of polarimetric amplitudes. It is, therefore, natural to select the regions based on the parameters composing the polarimetric covariance matrix of the data. Two methods for selecting these parameters are discussed in this section. One is supervised, and the other is unsupervised.

If the natural regions of the image are known in advance, for example, by coregistering the data with a ground map of the terrain cover, training areas may be selected to estimate the covariance matrix of each region as in [9]. A large number of elements is usually necessary to correctly estimate these parameters as speckle biases

the statistics of the data. The segmentation results are also quite sensitive to the selected set of training areas and a series of trials and errors is often required to obtain satisfactory results. More sophisticated training sets and training algorithms may also be necessary to account for a variability of the polarimetric characteristics of a region with the incidence angle due to changes in terrain slope or differences in range location within the image.

When training areas are not available, clustering techniques may help select the regions. There is a considerable interest in performing an unsupervised selection of the regions as: 1) the selection of training areas can rapidly become costly and time consuming; 2) clustering can give some meaningful insights into the dimensionality, nature, and structure of the data; 3) systems of automated analysis of a large volume of polarimetric data at high data rates need to be able to work with little or no operator supervision. A method is proposed in [24] based on the multidimensional clustering of the logarithm of the parameters composing the covariance matrix. The following polarimetric feature vector is defined

$$x_C = \begin{pmatrix} \sigma_{HH} \\ \sigma_{HV} \\ \sigma_{VV} \\ \sigma_{|HHVV^*|^{1/2}} \\ 10 \frac{\phi_{HHVV}}{\log(10)} \end{pmatrix} \quad (24)$$

where, for instance, $\sigma_{HV} = 10 \log_{10} (\langle |HV|^2 \rangle)$. The first three components correspond to the backscatter cross section of the area in decibels at different linear polarizations. The last two components are proportional to the real and imaginary parts of the logarithm base ten of the complex correlation function between HH and VV . One measures the magnitude of the correlation between HH and VV , the other measures the phase difference. For natural targets, the first four components have a typical dynamical range of about 30 dB, whereas the last one has a dynamical range of 27.2 dB as $\phi_{HHVV} \in [-\pi, +\pi]$. An Euclidean distance is used to measure the separation between polarimetric feature vectors.

The advantages of operating in the log domain compared to the linear domain are that weighting of the different channels is not necessary and speckle does not bias the selection of the cluster centers [24]. Furthermore, the decibels unit is a convenient and commonly used measure of the backscatter cross section of natural targets. Given the polarimetric feature vectors (24) of a small number (i.e., a few percent) of points uniformly distributed across the polarimetric data array, the ISODATA clustering routine [25] is used to estimate the polarimetric cluster centers from the iteratively determined sample means. Among the several input parameters needed to guide clustering [26], we kept constant and minimum number of samples

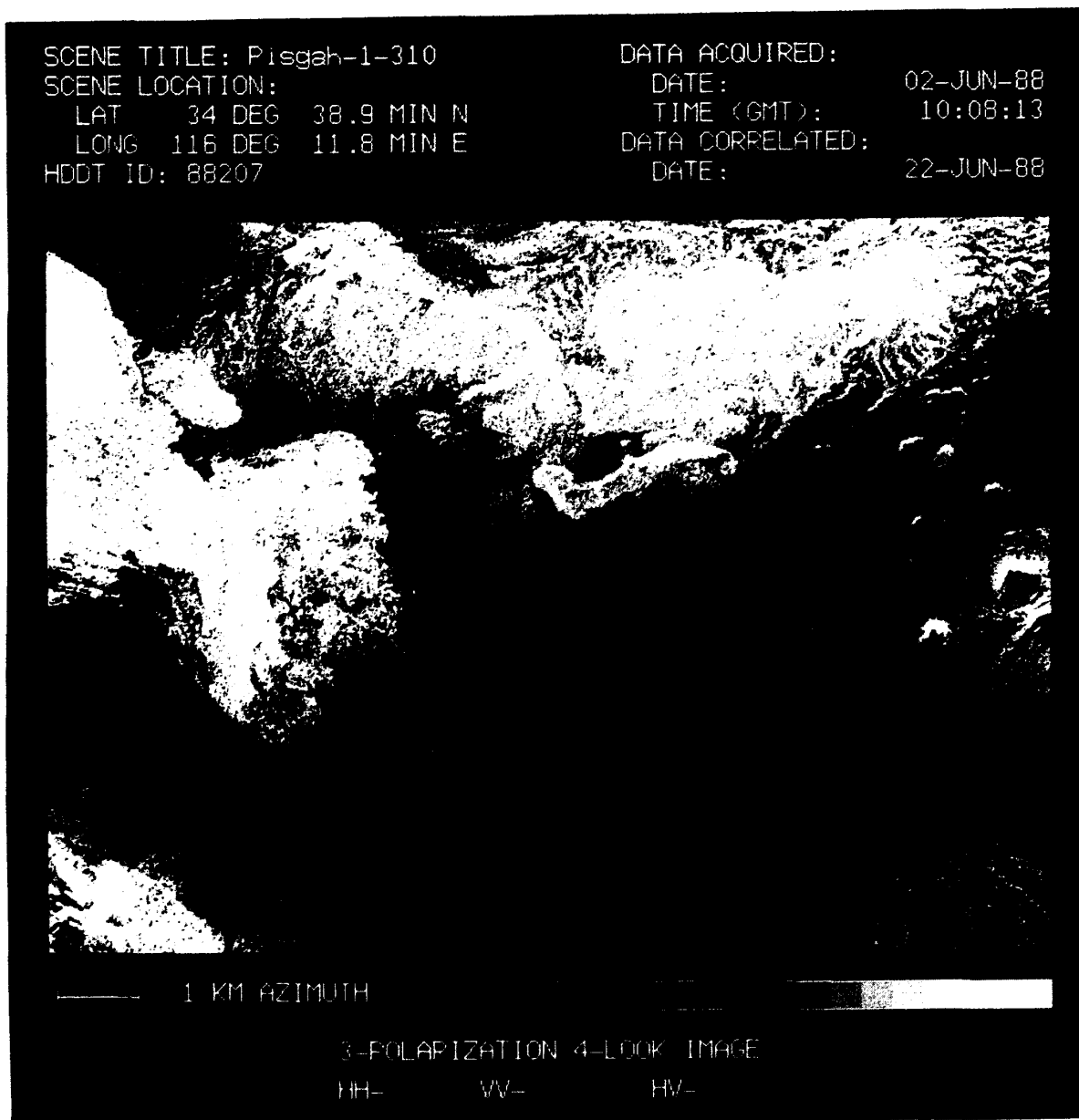
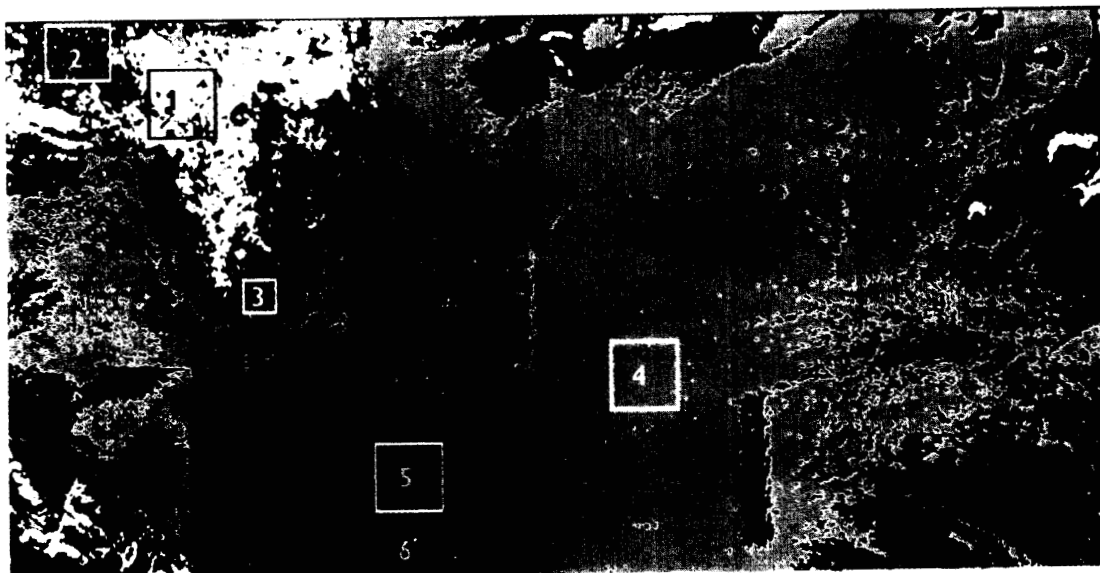


Fig. 2. Color overlay at three polarizations (HH is red, HV is green, and VV is blue) and L-band frequency of a four look image of the Pisgah scene in the Mojave desert, CA.

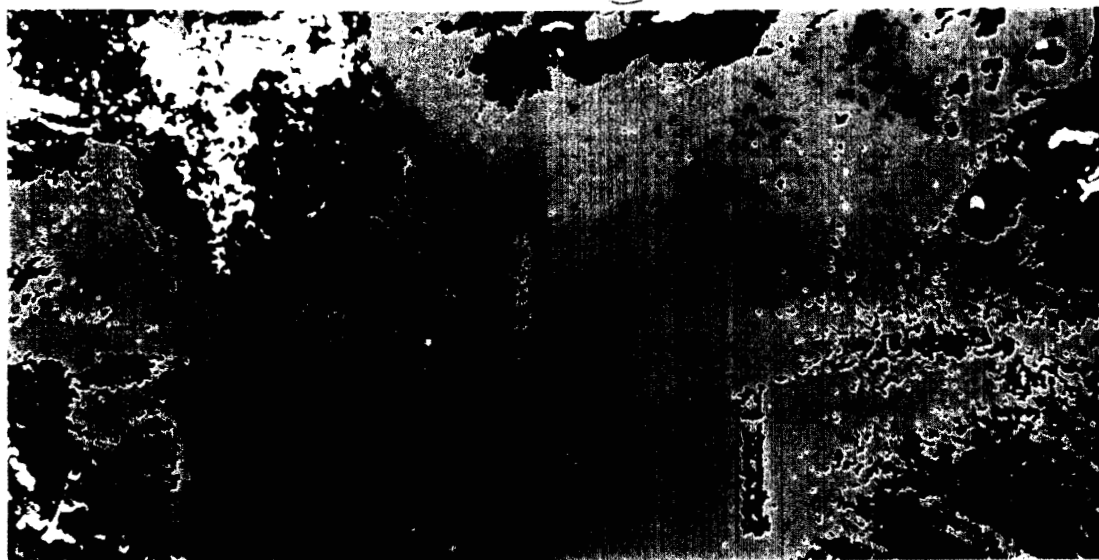
per cluster $\theta_N = 5$, the maximum number of pairs of clusters which can be lumped $L = 20$, the maximum number of iterations $I = 100$, and the splitting parameter $\gamma = 0.5$. The other parameters, K , the expected number of cluster centers, θ_s , the standard deviation parameter, and θ_c , the lumping parameter are application dependent; but in the experimental results discussed in Section VII, only a limited knowledge of the scene characteristics was necessary to manually select these parameters.

TABLE I
 POLARIMETRIC CHARACTERISTICS OF THE TRAINING AREAS. PISGAH SCENE—L-BAND

Training Area	σ_{HH} (dB)	σ_{HV} (dB)	σ_{VV} (dB)	$\sigma_{ HHVV ^{1/2}}$ (dB)	ϕ_{HHVV} (rad)
Phase II lava	-8.0	-17.7	-8.5	-9.8	0.01
Phase III lava	-9.5	-22.2	-10.2	-10.7	0.01
Phase I lava	-16.0	-26.9	-15.3	-16.9	-0.16
Alluvial fan	-23.8	-34.4	-22.8	-24.7	-0.03
Dry lake bed	-29.2	-41.5	-28.0	-29.6	-0.05



(a)



(b)

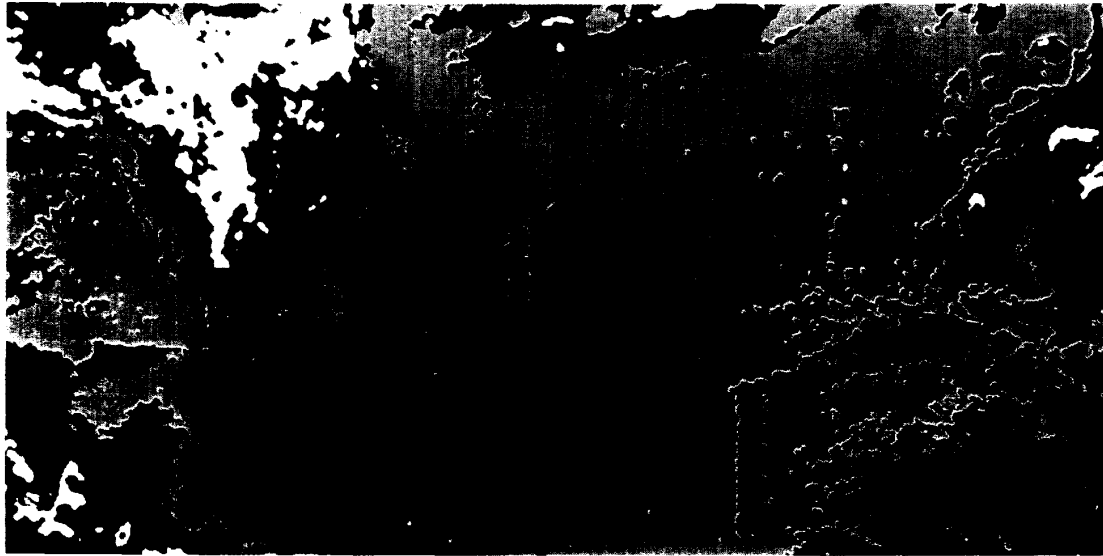
Fig. 3. Supervised classification of the Pisgah scene using the complete polarimetry. The five training areas outlined in (a) are: (1) phase II lava; (2) phase III lava; (3) phase I lava; (4) alluvial fan; (5) dry lake bed. (6) is a man made corner reflector. In the segmentation maps, these areas are, respectively, colored in white, brown, red, green, and blue. (a) ML classification map along with the location of the five training areas. (b) ICM classification map. (c) MAP classification map.

VII. EXPERIMENTAL RESULTS

The performance of the ML polarimetric classifier was studied by Kong *et al.* [9] using both simulated polarimetric data and theoretical analysis. It was shown that fully polarimetric data (i.e., HH , HV , VV) always yield the best results compared to any subset of the complete polarimetry such as single channels (e.g., HH), channel ratios (e.g., HH/VV), or phase differences (e.g., ϕ_{HHVV}). The performance of the MAP classifier was evaluated in

TABLE II
CLASSIFICATION ACCURACY IN PERCENT OF THE TRAINING AREAS. PISGAH
SCENE—L-BAND

Training Area	No.	ML	ICM	MAP
Phase II lava	1	86.82	93.16	97.63
Phase III lava	2	80.67	89.09	95.81
Phase I lava	3	87.51	89.59	91.47
Alluvial fan	4	99.50	99.95	100.00
Dry lake bed	5	94.21	95.08	96.05
Total		89.74	93.37	96.18



(c)

Fig. 3. (Continued.)

TABLE III
POLARIMETRIC CHARACTERISTICS OF THE CLUSTER CENTERS. PISGAH
SCENE—L-BAND

Cluster	σ_{HH} (dB)	σ_{HV} (dB)	σ_{VV} (dB)	$\sigma_{ HHVV ^{1/2}}$ (dB)	ϕ_{HHVV} (rad)	Nature
1	-8.9	-19.4	-9.4	-10.5	0.02	Phase II lava
2	-13.2	-24.2	-13.2	-14.4	0.11	Phase III lava
3	-17.7	-29.1	-17.1	-18.6	0.15	Phase I lava
4	-20.9	-32.7	-20.1	-21.7	0.09	Alluvial fan 1
5	-23.7	-36.3	-22.9	-24.4	0.04	Alluvial fan 2
6	-28.2	-41.0	-27.0	-28.8	0.05	Dry lake bed

TABLE IV
POLARIMETRIC CHARACTERISTICS OF THE TRAINING AREAS. FLEVLAND
SCENE—L-BAND

Training Area	σ_{HH} (dB)	σ_{HV} (dB)	σ_{VV} (dB)	$\sigma_{ HHVV ^{1/2}}$ (dB)	ϕ_{HHVV} (rad)
Potatoes	-8.6	-16.3	-9.0	-11.3	0.12
Stem Beans	-9.1	-19.2	-11.4	-16.3	1.44
Forest	-9.9	-15.1	-9.7	-18.5	0.37
Red Beet	-11.4	-19.5	-11.5	-13.5	-0.14
Peas	-11.4	-21.4	-9.8	-12.0	-0.24
Beet	-13.0	-21.1	-13.6	-15.8	-0.13
Bare Soil	-14.0	-25.2	-12.3	-14.0	-0.19
Lucerne	-16.1	-26.0	-18.2	-27.7	0.11
Winter Heat	-17.4	-26.8	-14.2	-18.8	-0.50
Grass	-18.2	-28.7	-18.6	-21.2	-0.47
Flax	-20.3	-35.7	-17.2	-19.2	-0.17
Summer Barley	-20.3	-28.9	-19.6	-23.5	-0.43
Water	-23.2	-36.9	-16.3	-20.2	-0.01

[7] using simulated single look single polarization SAR complex data as a function of the contrast between regions, the clustering parameter, the size of the neighborhood window, the spatial variability of the signal, and the number of regions. The study is not repeated here using simulated polarimetric data as the only difference is in the distribution of the radar measurements. In this section, experimental results are presented using real multilook polarimetric SAR complex data.

A. Classification of Fully Polarimetric Data

Fig. 2 shows a color overlay at L-band frequency and three polarizations (HH , HV and VV are, respectively, encoded in red, green, and blue) of the Pisgah scene in the Mojave Desert, CA, acquired by the NASA/JPL multi-frequency polarimetric aircraft SAR during the MFE Ex-

periment [27]. The saturation of each color is proportional to the intensity of the signal at that polarization and the average intensities of the different polarizations are set to the middle of the display dynamic range. The image is 4-look and 750 by 1024 pixels in size. Pixel spacing is 6.66 m in range (top to bottom in Fig. 2(a)), and 12.01 m in azimuth. The radar moved from right to left and the illumination direction is from the top. The scene contains various geological surfaces of different ages [28] which can be divided up into five main classes of terrain cover: phase I lava, phase II lava, phase III lava, alluvial fan, and dry lake bed. For each class of terrain cover, a training area was selected in the image. The average polarimetric characteristics of the training areas are indicated in Table I.



(a)



(b)

Fig. 4. Unsupervised segmentation of the Pisgah scene based on the six cluster centers of Table III and using the complete polarimetry. The regions corresponding to cluster one to six are respectively colored in white, brown, red, light green, dark green, and blue. (a) ML segmentation map. (b) MAP segmentation map.

These characteristics were used to generate the supervised ML classification map shown in Fig. 3(a) along with the location of the training areas. The image is 512 by 1024 in size. The first 256 records of the original scene have not been classified to reduce the computational burden, and also because they correspond to a portion of the image where radar backscatter fluctuations with the incidence angle are more significant and impair a segmenta-

tion scheme that does not account for incidence angle effects. Near range data are also affected by radar ambiguities that decrease the radiometric fidelity of the data.

To evaluate the quality of the results, the classification accuracy of the training areas is computed. Although we would prefer to compute the classification accuracy of the entire scene, it is not possible as ground truth information



Fig. 5. Color overlay of HH (red), HV (green), and VV (blue) at L-band frequency of a four look image of the Flevoland scene in The Netherlands.

is limited to a few large areas and does not permit an accurate pixel by pixel classification of the image. Collecting extensive ground truth information is, in general, very expensive and we do not have SAR data for which it is available.

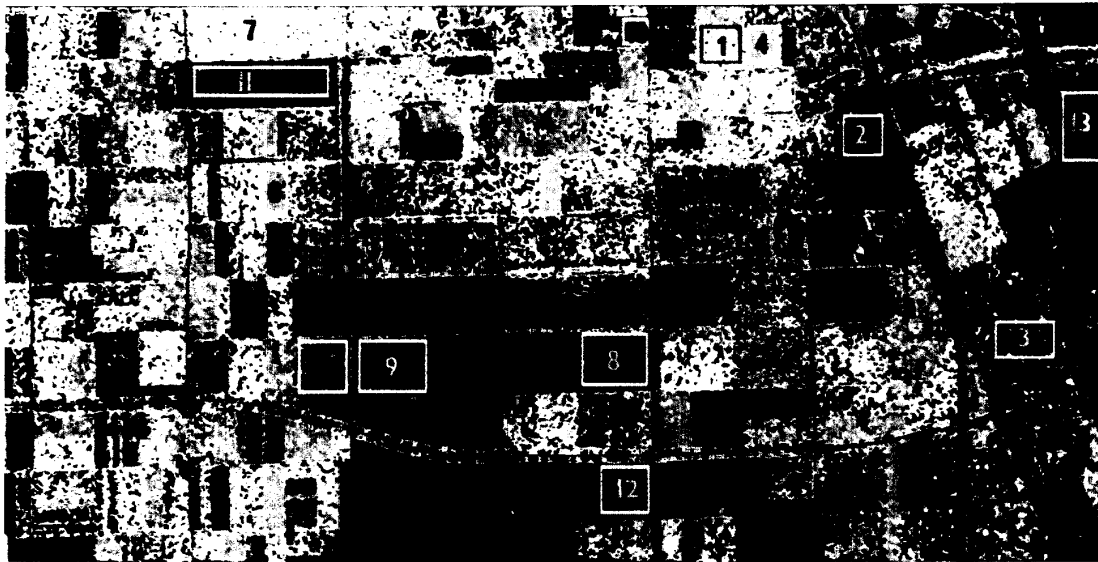
The classification accuracies of the training areas of Fig. 3(a), given in Table II, indicate that the different types of terrain cover are correctly separated. The ICM and MAP supervised classification maps are shown in Fig. 3(b) and (c), respectively. Classification accuracy is improved by 3.6% using the ICM method and by 6.4% us-

ing the MAP method. As expected, the MAP method performs better than the ICM method, although the segmentation maps look rather similar in this example.

The next figures show the segmentation maps resulting from an unsupervised selection of the polarimetric characteristics of the regions. An array of 51 by 101 elements extracted from the polarimetric data was clustered using $K = 6$ and $\theta_c = \theta_s = 3$ dB. The characteristics of the six cluster centers are given in Table III. The clusters have a good degree of homogeneity as the standard deviation of their elements is less than 2 dB and are well separated as

TABLE V
CLASSIFICATION ACCURACY IN PERCENT OF THE TRAINING AREAS.
FLEVOLAND SCENE—L-BAND

Training Area	No.	ML	ICM	MAP
Potatoes	1	92.30	100.00	100.00
Stem Beans	2	97.81	97.52	100.00
Forest	3	79.50	82.86	100.00
Red Beet	4	74.97	84.29	99.66
Peas	5	86.38	95.18	100.00
Beet	6	85.16	89.87	99.47
Bare Soil	7	92.77	99.02	100.00
Lucerne	8	96.86	99.55	100.00
Winter Heat	9	93.14	98.45	100.00
Grass	10	91.30	100.00	100.00
Flax	11	98.46	99.29	100.00
Summer Barley	12	81.24	88.42	96.85
Water	13	97.32	97.19	97.46
Total		89.79	94.74	99.50



(a)

Fig. 6. Supervised classification of the Flevoland scene using the complete polarimetry. The thirteen training areas in (a) correspond to: (1) potatoes; (2) stem beans; (3) forest; (4) red beet; (5) peas; (6) beet; (7) bare soil; (8) Lucerne; (9) winterheat; (10) grass; (11) flax; (12) summerbarley; (13) water. (a) ML classification map along with the location of the thirteen training areas. (b) ICM classification map. (c) MAP classification map.

the distance between the closest cluster centers is 5.9 dB. Clustering appears to be mainly driven by the radiometric information contained in the first three components of the polarimetric feature vector as the fourth component corresponds to a magnitude of the normalized correlation coefficient between HH and VV of about 0.74 for all clusters, and the fifth component is mostly zero. Indeed, an examination of the data indicates that the $HH - VV$ correlation coefficient is a poor discriminant (e.g., Table I), and that the phase difference is close to zero almost everywhere in the image. The ML and MAP segmentation maps shown in Fig. 4(a) and (b), respectively, were generated using the polarimetric characteristics of the cluster centers as the polarimetric characteristics of the regions. The

clustering routine is clearly able to separate the different types of terrain cover outlined in the previous maps. The MAP method produces better looking and more homogeneous regions than the ML method, yet, as opposed to what would be expected with a straightforward box filtering technique, detection accuracy is not impaired as the metallic trihedral corner reflectors (strong return in the bottom center of Fig. 2) and other small features (upper right portion of the image) about a few pixels wide are still present after optimization of the region labels.

The next example addresses the case of a larger number of classes. The data are 4-look fully polarimetric SAR data of the agricultural fields of Flevoland, The Netherlands, acquired by the NASA/JPL aircraft SAR. A color



(b)



(c)

Fig. 6. (Continued.)

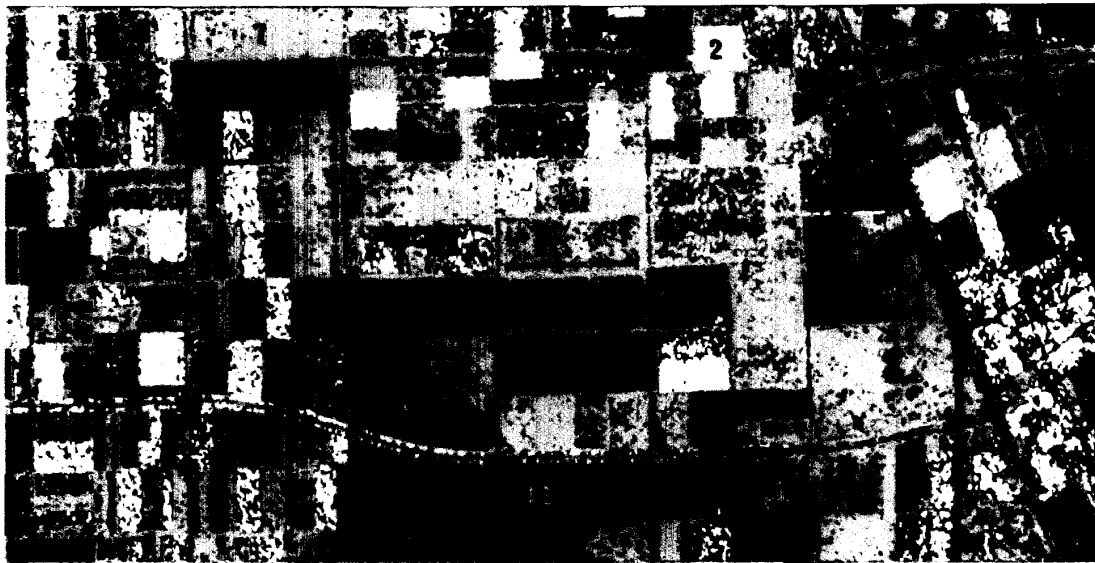
overlay at L-band frequency and three polarizations of the SAR data are shown in Fig. 5. A large variety of vegetation types and crops are present in the scene, along with seawater, roads, and inhabited areas. The site has been used for calibration studies and multitemporal monitoring of crops [29], and ground truth data are available for a portion of the image. Yet, such information must be used with care as crops may have grown between the collection of ground truth data and the SAR overflight, and some fields may have likely been harvested. The polarimetric characteristics of thirteen different types of terrain cover

selected across the scene, and for which we have good confidence in the ground truth data, are given in Table IV.

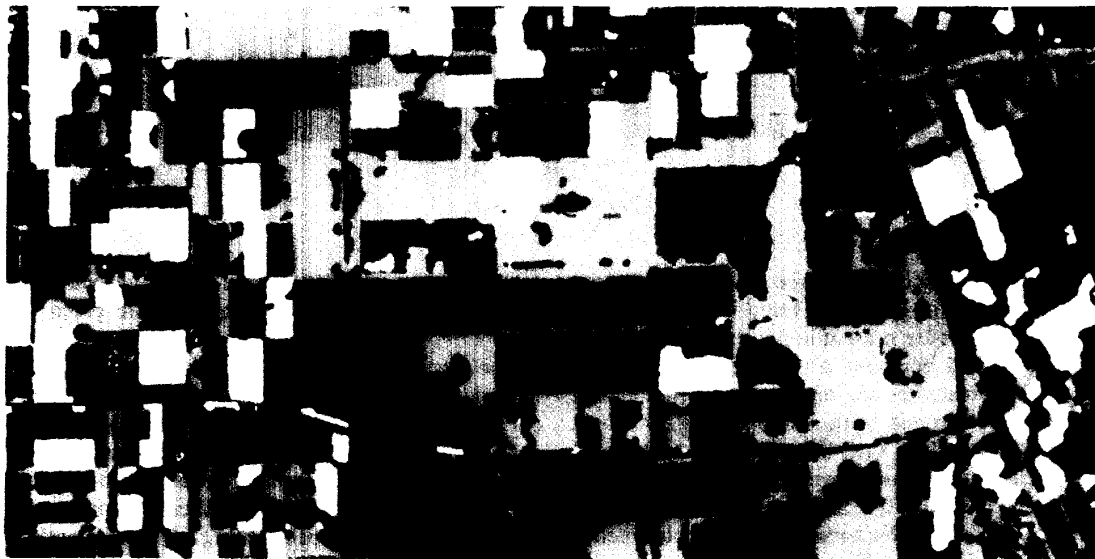
The resulting ML classification map is shown in Fig. 6(a) along with the location of the training areas. Again, only the last 512 records of the original scene have been classified. The result appears noisy although the classification accuracy of the training areas, given in Table V, is high. The ICM and MAP classification maps, shown in Fig. 6(b) and (c) respectively, are significantly better. The MAP method leads to an overall classification accu-

TABLE VI
POLARIMETRIC CHARACTERISTICS OF THE CLUSTER CENTERS. FLEVLAND SCENE—L-BAND

Cluster	σ_{HH} (dB)	σ_{HV} (dB)	σ_{VH} (dB)	$\sigma_{ HHVV+ ^{1/2}}$ (dB)	ϕ_{HHVV} (rad)	Nature
1	-2.6	-19.4	-9.1	-8.6	2.08	Man made targets
2	-9.9	-16.9	-10.2	-13.0	0.13	Forest + Potatoes
3	-10.3	-20.2	-11.8	-18.0	1.63	Stem Beans
4	-11.3	-17.3	-11.5	-17.0	0.13	Forest
5	-12.8	-21.5	-11.9	-14.5	-0.19	Red Beet + Peas + Beet
6	-14.0	-21.4	-14.2	-19.0	-0.09	Beet
7	-15.2	-25.1	-13.0	-15.8	-0.28	Bare Soil
8	-16.5	-25.8	-17.3	-24.5	-0.45	Lucerne
9	-17.2	-26.7	-15.6	-19.0	-0.40	Winter Heat + Grass
10	-17.8	-28.7	-18.4	-28.2	1.21	N.A.
11	-19.4	-29.0	-20.6	-28.6	-2.32	N.A.
12	-20.1	-29.3	-18.6	-22.2	-0.43	Grass + Summer Barley
13	-22.2	-35.8	-17.5	-20.6	-0.17	Flax + Water



(a)



(b)

Fig. 7. Unsupervised segmentation of the Flevoland scene based on the thirteen clusters of Table VI and using the full polarimetry. An index overlaid on top of the segmentation map indicates the coloring of the regions corresponding to each cluster center. For example, index "2" is colored in white and corresponds to cluster two. (a) ML segmentation map along with the index of the clusters. (b) MAP segmentation map.

TABLE VII
CLASSIFICATION ACCURACY IN PERCENT OF THE TRAINING AREAS. ML CLASSIFIER—
FLEVOLAND SCENE—L-BAND

Training Area	No.	Full Pol.	HH	HV	VV	HH + HV	VV + HV	HH + VV
Potatoes	1	92.30	54.63	60.03	55.94	65.03	67.32	90.34
Stem Beans	2	97.81	19.28	42.51	32.00	70.27	46.09	87.65
Forest	3	79.50	32.01	57.30	9.59	66.83	61.04	67.22
Red Beet	4	74.97	23.01	25.36	15.37	54.55	34.68	64.76
Peas	5	86.38	27.09	56.41	24.82	55.08	83.97	78.61
Beet	6	85.16	36.89	30.76	34.22	68.09	86.49	73.60
Bare Soil	7	92.77	44.71	47.98	30.25	66.67	68.55	91.10
Lucerne	8	96.86	51.62	22.04	22.50	52.63	76.91	95.43
Winter Heat	9	93.14	33.50	42.11	44.34	50.69	79.70	90.61
Grass	10	91.30	29.68	76.94	18.15	59.74	48.77	88.09
Flax	11	98.46	20.41	48.00	21.96	70.19	56.00	97.66
Summer Barley	12	81.24	43.10	0.00	70.70	79.38	66.62	81.40
Water	13	97.32	83.85	73.65	35.01	85.49	77.64	97.14
Total		89.79	46.45	44.85	31.91	64.97	65.68	84.86

TABLE VIII
CLASSIFICATION ACCURACY IN PERCENT OF THE TRAINING AREAS. MAP CLASSIFIER—FLEVOLAND SCENE—
L-BAND

Training Area	No.	Full Pol.	HH	HV	VV	HH + HV	VV + HV	HH + VV
Potatoes	1	100.00	36.77	55.61	100.00	100.00	100.00	100.00
Stem Beans	2	100.00	26.44	100.00	22.94	99.85	73.41	100.00
Forest	3	100.00	17.63	87.11	74.32	94.55	98.13	99.78
Red Beet	4	99.66	23.01	71.26	99.89	100.00	0.00	99.55
Peas	5	100.00	62.08	50.12	50.35	100.00	100.00	100.00
Beet	6	99.47	98.31	0.00	100.00	95.29	100.00	91.64
Bare Soil	7	100.00	43.38	49.63	39.70	99.00	93.84	100.00
Lucerne	8	100.00	91.35	52.18	55.32	98.46	100.00	99.79
Winter Heat	9	100.00	65.25	94.06	35.60	96.25	100.00	99.90
Grass	10	100.00	31.19	100.00	23.25	100.00	100.00	100.00
Flax	11	100.00	15.50	27.85	38.07	97.93	80.27	99.76
Summer Barley	12	96.85	96.64	6.20	95.97	100.00	100.00	97.31
Water	13	97.46	98.23	77.19	69.07	91.38	79.64	97.23
Total		99.50	54.29	59.32	61.88	97.90	86.56	98.84

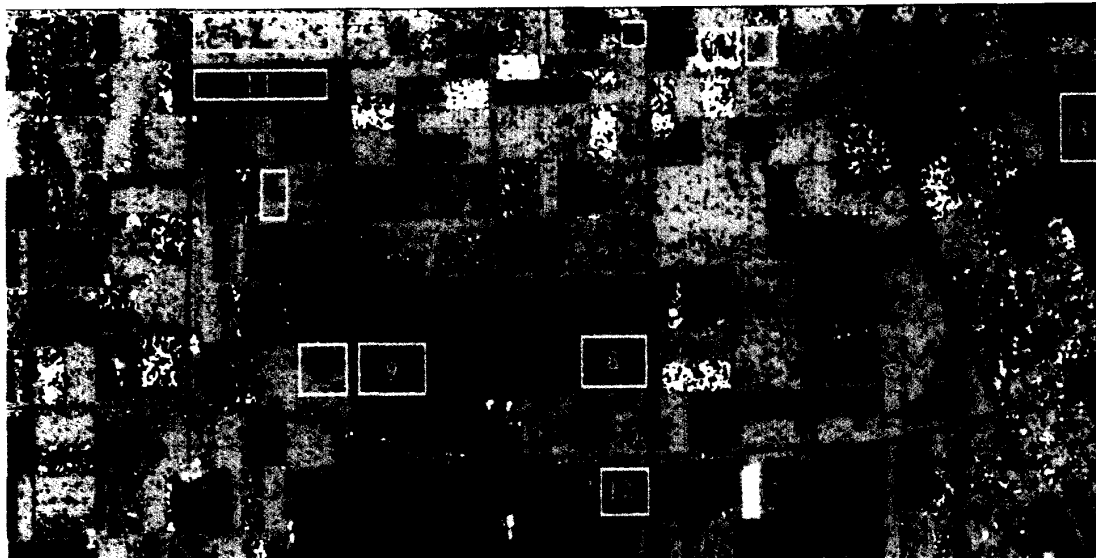
accuracy improved by 9.7% and close to a perfect score whereas the ICM method only produces a 5% increase in classification accuracy. Hence, the difference in classification accuracy between MAP and ICM increases with the number of regions. As mentioned in Section V, a probable reason may be that ICM gets easily stuck in poorer local minima as the energy function becomes more complicated.

These results were also computed to those obtained using the method described in [12], which is similar to ICM, but does not use a MRF for representing the distribution of the region labels, and allows the neighborhood window N_s to contain a number of elements roughly equal to ten times the number of possible classes. As the number of elements is too large to maintain minimum classification error at the region boundaries, a comparison of the three methods was performed using a 3 by 3 neighborhood window in each case. The method presented in [12] resulted in a 93.7% classification accuracy of the training areas, which is comparable to ICM (Table V), but 5.8% worse than MAP.

As in the previous example, an array of 51 by 101 elements extracted from the polarimetric data was clustered using $K = 13$ and $\theta_c = \theta_s = 3.5$ dB. The polarimetric characteristics of the thirteen clusters are indicated in Ta-

ble VI. The standard deviation of their elements is less than 3.2 dB and the cluster centers are separated by more than 4.4 dB. Again, the radiometric information of the first three components seem to determine clustering, except for cluster one and three which have a significant contribution from the phase difference term. A comparison of the resulting segmentation maps with the ground truth data reveals that cluster one corresponds to the trihedral metallic corner reflectors deployed in the area for calibration purposes and other unidentified man-made structures characterized by a highly polarized high backscatter return. Cluster three corresponds to areas covered with stem beans where the large nonzero phase difference between the HH and VV channels could be attributed to the particular structure of the stem beans, that are vertically oriented scatterers, thereby generating a difference in wave velocity between the horizontal and vertical directions as in the corn fields studied in [30]. The ML and MAP segmentation maps are shown in Fig. 7(a) and (b), respectively. The MAP technique improves the separability of the regions and their degree of homogeneity. Fine structures such as roads and corner reflectors are still present after optimization of the region labels, and regions have sharp and straight boundaries.

Based on the polarimetric distance between the cluster



(a)



(b)

Fig. 8. Supervised classification of the Flevoland scene using the thirteen training areas of Fig. 6(a) and the HH channel. Coloring of the regions is the same as in Fig. 6. (a) ML classification map along with the location of the thirteen training areas. (b) MAP classification map.

centers and the mean polarimetric characteristics of each training area, a correspondence was established between clusters and natural classes as shown in Table VI. In this example, there is not a one to one correspondence between clusters and classes of terrain cover. Classes only separated by a few decibels (Table V) are merged into one cluster. Yet, in the absence of extensive ground truth data, the unsupervised selection of the regions provides useful information about the polarimetric feature space, i.e., the regions naturally separated by the radar, that is consistent with the spatial structure of the scene (rectangular ho-

mogeneous fields of Fig. 7(b), and that may be useful to the analyst. For instance, cluster ten and eleven map two homogeneous fields that were misclassified as a mixture of different crops (Lucerne, summer barley, and grass) in Fig. 6(b) which is probably incorrect.

B. Classification of Single and Dual Polarization Data

To illustrate the effect of reducing the dimension of the polarimetric measurement vector (1) on segmentation accuracy, a supervised classification of the data was per-



(a)



(b)

Fig. 9. Supervised classification of the Flevoland scene using the thirteen training areas of Fig. 6(a) and the HH and HV channels. Coloring of the regions is the same as in Fig. 6. (a) ML classification map along with the location of the thirteen training areas. (b) MAP classification map.

formed using various combinations of the polarimetric channels. For each combination, (9) was modified accordingly to account for a reduction in the number of components of the polarimetric measurement vector. The classification accuracy results are indicated in Tables VII and VIII for the Flevoland data. As discussed in [9], the fully polarimetric data always yield the best results when the ML method is used (Table VII). Classification accuracy is improved by more than 40% compared to single polarization classification schemes. When the MAP method is used the fully polarimetric classifier is also

much better than any single channel classifiers (Table VIII). For illustration, the ML and MAP classification maps using the HH channel are given in Fig. 8(a) and (b), respectively. In this case where the likelihood function U_1 is a poor discriminant, the smoothing effect of the region labeling optimization process is more apparent.

On the other hand, classifiers based on the combination of two channels yield results, that are considerably closer to that of the fully polarimetric classifier, especially when the MAP algorithm is used. An example is given on Fig. 9 with the MAP classification map using the HH and VV

TABLE IX
CLASSIFICATION ACCURACY IN PERCENT OF THE TRAINING AREAS. ML CLASSIFIER—PISGAH SCENE—L-BAND

Training Area	No.	Full Pol.	HH	HV	VV	HH + HV	VV + HV	HH + VV
Phase II lava	1	86.82	56.70	84.88	60.94	85.08	71.86	79.52
Phase III lava	2	80.67	62.20	73.23	61.85	78.22	58.57	77.30
Phase I lava	3	87.51	88.35	67.85	91.78	84.29	83.87	89.59
Alluvial fan	4	99.50	98.14	90.12	97.71	98.46	96.30	99.70
Dry lake bed	5	94.21	92.86	96.38	92.10	94.65	93.67	92.43
Total		89.74	79.65	82.50	80.88	88.14	80.86	87.71

TABLE X
CLASSIFICATION ACCURACY IN PERCENT OF THE TRAINING AREAS. MAP CLASSIFIER—PISGAH SCENE—L-BAND

Training Area	No.	Full Pol.	HH	HV	VV	HH + HV	VV + HV	HH + VV
Phase II lava	1	97.63	74.50	100.00	88.96	98.76	99.73	98.95
Phase III lava	2	95.81	61.70	97.57	94.96	96.50	97.54	96.66
Phase I lava	3	91.47	94.90	90.32	97.81	91.05	92.30	92.72
Alluvial fan	4	100.00	100.00	98.11	100.00	100.00	100.00	100.00
Dry lake bed	5	96.05	97.08	99.40	96.43	97.94	97.19	96.10
Total		96.18	85.64	97.08	95.63	96.85	97.35	96.89

channels. The three possible dual polarization combinations lead to nearly similar performances although the combination ($VV + HV$) completely misses the red beet training area.

Similar observations can be made from the results obtained with the Pisgah scene (Tables IX and X). Single polarization classifications are considerably better in that example as the HV channel alone produces the best overall classification accuracy of the training areas. Although such results are uncommon, several factors may explain why single or dual polarization systems may sometimes outperform fully polarimetric systems. Firstly, as the dimension of the radar measurements decreases, the energy function U_1 will (in general) decrease and U_2 remain the same leading to more smoothing of the region labels. Since the training areas are assumed to be perfectly homogeneous, additional smoothing may in some situations help improve the classification accuracy. Secondly, in real systems, noise perturbations in polarimetric channels may be uneven so that confusion between the classes may actually increase with the number of polarimetric channels. Thirdly, training areas as seen by the fully polarimetric radar may not be as homogeneous as single polarization radars seem to indicate. The assumption that training areas are perfectly homogeneous is indeed a major flaw of this method of comparison between different algorithms.

The main observation remains that although fully polarimetric SAR data yield the best segmentation results over all polarization combinations, dual polarization; and that sometimes single polarization SAR data may produce the same level of classification accuracy. Fully polarimetric SAR data are still essential to completely interpret and understand the scattering mechanisms of the imaged surface, but these few examples show that classification algorithms for natural scenes could probably accommodate for a reduction in the dimension of the polarimetric

SAR measurements. Similarly, model inversion techniques may be able to accommodate for the use of only one or two polarimetric channels to infer useful geophysical parameters from the surface in given applications [31]. As single and even dual polarization radar systems are considerably less complex and cheaper than fully polarimetric radar systems, such a possibility offers interesting technological prospects.

VIII. CONCLUSIONS

A method based on a representation of the posterior distribution of the region labels, given the polarimetric measurements, has been presented for segmenting multilook polarimetric SAR complex data. The maximization of this distribution produces the most likely region labeling given the observed polarimetric SAR complex data. Results using real multilook polarimetric SAR data show a 10–20% improvement in segmentation accuracy of the MAP method compared to that of the ML method [9], and demonstrate the importance of using correlative information from neighboring pixels to improve the segmentation accuracy of the data. ICM, a fast alternative to MAP, appears to be a reasonable approximate solution that could be used during optimization of the selection of the regions leaving the use of the MAP method for the final iteration. The rapid progress of computer technology may also soon render the MAP method itself practical and computationally inexpensive.

Comparisons of classification results using single, dual, and full polarization data indicate that dual, and sometimes single, polarization SAR data may yield segmentation results nearly equivalent to that of fully polarimetric SAR data. More studies are needed to determine the best compromise between classification accuracy and complexity of the imaging and processing systems in various

applications, at different frequencies, and using a larger data set.

Further work is necessary to develop incidence angle dependent segmentation techniques that account for a strong variability of the polarimetric characteristics of natural targets with the incidence angle of the radar signal. The effect of a significant spatial variability of the SAR signal on classification accuracy must also be investigated using real image data.

ACKNOWLEDGMENT

The authors would like to thank Antony Freeman, Peter Hoogeboom, and John Villasenor for the use of the Flevoland data, Jakob van Zyl for useful and stimulating discussions, Pascale Dubois for her insightful comments, Ronald Kwok for his support, and the people involved in the Jet Propulsion Laboratory SAR program who operated the imaging polarimeter and processed the data used in this paper. They would also like to thank the anonymous referees that reviewed this paper for their many constructive comments.

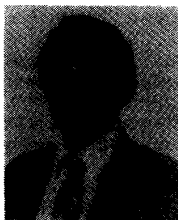
REFERENCES

- [1] F. T. Ulaby and C. Elachi, *Radar Polarimetry for Geoscience Applications*. Norwood, MA: Artech House, 1990.
- [2] H. A. Zebker, J. J. van Zyl, and D. Held, "Imaging radar polarimetry from wave synthesis," *J. Geophys. Res. B*, vol. 92, pp. 683-701, Jan. 1987.
- [3] J. J. van Zyl, "Unsupervised classification of scattering behavior using radar polarimetry data," *IEEE Trans. Geosci. Remote Sens.*, vol. 27, pp. 36-44, Jan. 1989.
- [4] A. C. Bovik, "On detecting edges in speckle imagery," *IEEE Trans. Acoust., Speech, Signal Processing*, vol. 36, pp. 1618-1627, Oct. 1988.
- [5] H. Derin, P. A. Kelly, G. Vezina, and S. G. Labitt, "Modeling and segmentation of speckled images using complex data," *IEEE Trans. Geosci. Remote Sens.*, vol. 28, pp. 76-87, Jan. 1990.
- [6] P. A. Kelly, H. Derin, and K. D. Hartt, "Adaptive segmentation of speckled images using a hierarchical random field model," *IEEE Trans. Acoust., Speech, Signal Processing*, vol. 36, pp. 1628-1641, Oct. 1988.
- [7] E. Rignot and R. Chellappa, "Segmentation of synthetic aperture radar complex data," *J. Opt. Soc. Amer., A*, pp. 1499-1509, Sept. 1991.
- [8] C. F. Burnette, P. C. Dubois, and J. J. van Zyl, "Segmentation of multifrequency polarimetric radar images to facilitate the inference of geophysical parameters," in *Proc. 1989 Int. Geoscience and Remote Sensing Symp.*, Vancouver, B.C., July 1989, pp. 30-33.
- [9] J. A. Kong, A. A. Swartz, H. A. Yueh, L. M. Novak, and R. T. Shin, "Identification of terrain cover using the optimum polarimetric classifier," *J. Electron. Waves Appl.*, vol. 2, pp. 171-194, Feb. 1988.
- [10] H. H. Lim, A. A. Swartz, H. A. Yueh, J. A. Kong, R. T. Shin, and J. J. van Zyl, "Classification of Earth terrain using polarimetric synthetic aperture radar images," *J. Geophys. Res., B*, vol. 94, pp. 7049-7057, June 1989.
- [11] H. A. Yueh, A. A. Swartz, J. A. Kong, R. T. Shin, and L. M. Novak, "Bayes classification of terrain cover using normalized polarimetric data," *J. Geophys. Res., B*, vol. 93, pp. 15 261-15 267, Dec. 1988.
- [12] J. J. van Zyl and C. F. Burnette, "Bayesian classification of polarimetric SAR images using adaptive a-priori probabilities," to be published.
- [13] B. S. Manjunath, T. Simchony, and R. Chellappa, "Stochastic and deterministic networks for texture segmentation," *IEEE Trans. Acoust. Speech, Signal Processing*, vol. 38, pp. 1039-1049, June 1990.
- [14] S. H. Yueh, J. A. Kong, J. K. Jao, R. T. Shin, and L. M. Novak, "K-distribution and polarimetric terrain radar clutter," *J. Electron. Waves Appl.*, vol. 3, pp. 747-768, Aug. 1989.
- [15] L. M. Novak, M. B. Sechtin, and M. J. Cardullo, "Studies of target detection algorithms that use polarimetric radar data," *IEEE Trans. Aerosp. Electron. Syst.*, vol. 25, pp. 150-165, Mar. 1989.
- [16] M. Borgeaud, R. T. Shin, and J. A. Kong, "Theoretical models for polarimetric radar clutter," *J. Electron. Waves Appl.*, vol. 1, pp. 67-86, Jan. 1987.
- [17] E. Rignot, "Segmentation of multifrequency and polarimetric synthetic aperture radar data," Ph.D. dissertation, Dep. of EE-Systems, Univ. of Southern California, Los Angeles, CA, May 1991.
- [18] P. Dubois, L. Norikane, J. van Zyl, and H. Zebker, "Data volume reduction for imaging radar polarimeter," in *Proc. IEEE AP-S Int. Symp.*, vol. III, San Jose, CA, June 1989, pp. 1354-1357.
- [19] R. Kinderman and J. L. Snell, *Markov Random Fields and Their Applications*. Providence, RI: Amer. Math. Soc., 1980.
- [20] J. Besag, "On the statistical analysis of dirty pictures," *J. Royal Statist. Soc., B*, vol. 48, pp. 259-302, Mar. 1986.
- [21] J. Marroquin, S. Mitter, and T. Poggio, "Probabilistic solution of ill-posed problems in computer visio," in *Proc. Image Understanding Workshop*, Miami Beach, FL, Dec. 1985, pp. 293-309.
- [22] J. J. Hopfield and D. W. Tank, "Neural computation of decisions in optimization problems," *Biol. Cybern.*, vol. 52, pp. 114-152, 1985.
- [23] S. Geman and D. Geman, "Stochastic relaxation, Gibbs distributions, and the Bayesian restoration of images," *IEEE Trans. Pattern Anal. Machine Intell.*, vol. PAMI-6, pp. 721-741, Nov. 1984.
- [24] E. Rignot, R. Chellappa, P. Dubois, R. Kwok, J. van Zyl, "Unsupervised segmentation of polarimetric SAR data using the covariance matrix," in *Proc. 1991 Int. Geoscience and Remote Sensing Symp.*, Espoo, Finland, June 1991, pp. 1813-1816.
- [25] G. H. Ball and D. J. Hall, "A clustering technique for summarizing multi-variate data," *Beh. Sci.*, vol. 12, pp. 153-155, 1974.
- [26] J. T. Tou and R. C. Gonzales, *Pattern Recognition Principles*. Reading, MA: Addison-Wesley, 1974, pp. 97-100.
- [27] S. Wall, "The Mojave field experiment: Precursor to the planetary test site," presented at 20th Ann. Meeting of the Div. of Planetary Science of the Amer. Astron. Soc., Austin, TX, Oct. 1985.
- [28] W. S. Wise, "Geological map of the Pisgah and Sunshine cone lava fields," NASA TL-11, 1966.
- [29] A. Freeman, J. C. Curlander, F. Heel, M. Zink, P. Hoogeboom, J. Groot, A. Dawkins, J. Baker, M. Reich, and H. Lentz, "Preliminary results of the multi-sensor, multipolarization SAR calibration experiments in Europe 1989," in *Proc. 1990 Int. Geoscience and Remote Sensing Symp.*, Maryland, VA, May 1990, pp. 783-786.
- [30] F. T. Ulaby, D. Held, M. C. Dobson, K. C. McDonald, and T. B. A. Senior, "Relating polarization phase difference of SAR signals to scene properties," *IEEE Trans. Geosci. Remote Sens.*, vol. GE-25, pp. 83-91, Jan. 1987.
- [31] J. J. van Zyl, Personal communication, Apr. 1991.



Eric Rignot was born in Chambon sur Lignon, France. He received the Engineer's diploma from the Ecole Centrale des Arts et Manufactures Paris in 1985, the M.S. degree in astronomy from the University of Paris VI in 1986, the M.S. degree in aerospace engineering and in electrical engineering in 1987 and 1988, respectively, and the Ph.D. degree in electrical engineering from the University of Southern California in 1991.

He was employed as a Research Assistant at the University of Southern California with the Department of Aerospace Engineering in 1986-1988. He then joined the Jet Propulsion Laboratory, California Institute of Technology, as a Member of the Technical Staff in the Radar Science and Engineering section. His current interests include multisensor image registration, SAR image geocoding, sea-ice classification from spaceborne data, multifrequency polarimetric SAR observations of sea- and glacier-ice, and monitoring of environmental conditions in the boreal forests using ERS-1 SAR data.



Rama Chellappa (F'91) was born in Madras, India. He received the B.S. degree in electronics and communication engineering from the University of Madras in 1975, the M.S. degree in electrical communication engineering from the Indian Institute of Science in 1977, and the M.S. and Ph.D. degrees in electrical engineering from Purdue University in 1978 and 1981, respectively.

During 1979-1981, he was a Faculty Research Assistant with the Computer Vision Laboratory, University of Maryland, College Park, MD. From 1981 to 1991, he was a Faculty member with the Department of Electrical Engineering-Systems, University of Southern California. From 1988 to 1990, he was also the Director of the Signal and Image Processing Institute at USC. In 1991, he became a Professor with the Department of Electrical Engineering, University of Maryland, where he is also associated with the Institute for Advanced Computer Studies, the Center for Automation Research, and the Department of Computer Science. He is a co-editor of two

volumes of selected papers on image analysis and processing, and of *Computer Vision, Graphics and Image Processing: Graphic Models and Image Processing*. His research interests include signal and image processing, computer vision, and pattern recognition.

Dr. Chellappa was the General Chairman for IEEE Computer Society Conference on Computer Vision and Pattern Recognition, San Diego, CA, June 1989 the IEEE Computer Society Workshop for AI for Computer Vision, and the Program Co-Chair for the NSF sponsored Workshop on Markov Random Fields. He has served as an Associate Editor for the IEEE TRANSACTIONS ON ACOUSTICS, SPEECH, AND SIGNAL PROCESSING, and currently serves as an Associate Editor for the IEEE TRANSACTIONS ON NEURAL NETWORKS and the IEEE TRANSACTIONS ON IMAGE PROCESSING. He has received the Jawaharla Nehru Memorial Award in 1975, from the Department of Education, India. In 1985, he received the NSF Presidential Young Investigator Award and the IBM Faculty Development Award. In 1990, he received the Excellence in Teaching Award from the School of Engineering, USC.